Miner Deposita (2012) 47:545–562
DOI 10.1007/s00126-011-0395-y

ARTICLE

Phosphorite-hosted zinc and lead mineralization in the Sekarna deposit (Central Tunisia)

Hechmi Garnit · Salah Bouhlel · Donatella Barca · Craig A. Johnson · Chaker Chtara

Received: 16 February 2010 / Accepted: 2 December 2011 / Published online: 17 December 2011

Abstract The Sekarna Zn–Pb deposit is located in Central Tunisia at the northeastern edge of the Cenozoic Rohia graben. Mineralization comprises two major ore types: (1) disseminated Zn–Pb sulfides that occur as lenses in sedimentary phosphorite layers and (2) cavity-filling zinc oxides (calamine-type ores) that crosscut Late Cretaceous and Early Eocene limestone. We studied Zn sulfide mineralization in the Saint Pierre ore body, which is hosted in a 5-m-thick sedimentary phosphorite unit of Early Eocene age. The sulfide mineralization occurs as replacements of carbonate cement in phosphorite. The ores comprise stratiform lenses rich in sphalerite with minor galena, Fe sulfides, and earlier diagenetic barite. Laser ablation–inductively coupled plasma mass spectrometry analyses of sphalerite and galena show a wide range of minor element contents with significant enrichment of cadmium in both sphalerite (6,000–20,000 ppm) and galena (12–189 ppm). The minor element enrichments likely reflect the influence of the immediate organic-rich host rocks. Fluid inclusions in sphalerite give homogenization temperatures of 80–130°C. The final ice melting temperatures range from −22°C to −11°C, which correspond to salinities of 15–24 wt. % NaCl eq. and suggest a basinal brine origin for the fluids. Sulfur isotope analyses show uniformly negative values for sphalerite (−11.2‰ to −9.3‰) and galena (−16‰ to −12.3‰). The $\delta^{34}S$ of barite, which averages 25.1‰, is 4‰ higher than the value for Eocene seawater sulfate. The sulfur isotopic compositions are inferred to reflect sulfur derivation through bacterial reduction of contemporaneous seawater sulfate, possibly in restricted basins where organic matter was abundant. The Pb isotopes suggest an upper crustal lead source.

Keywords Zn–Pb deposits · Sedimentary phosphorites · Sekarna · Central Tunisia

Editorial handling: B. Lehmann

H. Garnit (✉) · S. Bouhlel
Department of Geology, Faculty of Sciences of Tunis,
El Manar University,
2092 Tunis, Tunisia
e-mail: garnit1hechmi@yahoo.fr

S. Bouhlel
e-mail: salah.bouhlel@fst.rnu.tn

D. Barca
Department of Earth Sciences, University of Calabria,
via Ponte Bucci 4, Cubo 15B,
87036 Arcavacata di Rende (CS), Italy
e-mail: barca@unical.it

C. A. Johnson
U.S. Geological Survey,
MS 963, Box 25046, Denver, CO 80225, USA

C. Chtara
Groupe Chimique Tunisien (G.C.T.),
110, Rue Habib Chagra,
6002 Gabes, Tunisia

Introduction

The major Tunisian Pb–Zn–(Ba–F) deposits, which occur in carbonate rocks of Mesozoic to Tertiary age, are thought to have formed from orogenically driven brines that circulated through crystalline rocks and then ascended and reacted with fluids in overlying rocks during collision of the European and African plates (Rouvier et al. 1985; Bouhlel 2005). Although the major deposits are found in calcareous rocks, evidence from other Pb–Zn deposits in the Diapir Zone, including the well-studied Bougrine deposit, suggests that salt diapirism played an important role in the emplacement

of the deposits (Orgeval et al. 1989; Sheppard et al. 1996; Bouhlel et al. 2009).

The Sekarna Zn–Pb deposit is distinctive in that it occurs in sedimentary phosphorites of Early Eocene age. The setting thus differs from most other Tunisian ores, although it resembles the setting of Pb–Zn mineralization that has been found in the Oued El Abeid deposit in Central Tunisia (Fuchs 1973).

Following the discovery of Sekarna in 1906 (Sainfeld 1952), the area was explored and then mined from 1922 to 1948. Total production during this time was 4,540 tonnes of galena (2,600 t of Pb metal) and 22,000 tonnes of calamine (7,250 t of Zn metal). Mining activity focused on calamine and replacement galena ores in karstic cavities in Late Cretaceous and Early Eocene carbonates. Renewed interest, which has focused on the Saint Eugène mine, stems from recent advances in ore processing technologies and targets the non-sulfide Zn potential. Wide variation in the size of mineralized zones at Sekarna complicates the estimation of tonnage and grade for both the major and minor orebodies. Metal ratios vary from non-sulfide Zn-rich ore, which has Zn/(Zn+Pb) >0.73, to sulfidic Pb–Zn ore, which has Zn/(Zn+Pb) of about 0.35. Massive non-sulfide orebodies can reach 40,000 tonnes.

In this paper, we describe the tectonic and sedimentary setting of the Sekarna mineralization, the mineralogy and textures of the rocks, and the timing of mineralization relative to sedimentation. We also report fluid inclusion data which constrain the temperature and salinity of the mineralizing fluids, trace element data, and sulfur and lead isotope data, which constrain the sources of sulfur and metals and the mechanism of ore formation.

Geological setting

The Sekarna deposit is located in Central Tunisia, about 220 km southwest of Tunis and 20 km SW of Maktar (Fig. 1). This area was located on the southern margin of the Tethys Ocean during the Late Mesozoic and Early Cenozoic, a time when most of Tunisia was submerged, except for Djeffara Island to the south and Kasserine Island to the north (Sassi 1974; Burollet and Odin 1980; Chaabani 1995; Zaïer et al. 1998). The Sekarna area lay in the Northern Basin close to Kasserine Island (Fig. 2), which has been subaerially exposed since the Late Cretaceous (Sassi 1980; Béji-Sassi 1999; Zaïer 1999). Kasserine Island controlled sedimentation in the surrounding basins, which included phosphatic sediments in shallow waters (Bonnefous and Bismuth 1982; Zaïer et al. 1998). To the north, toward the continental margin, platform carbonates (Nummulitic facies) and pelagic carbonates (Globogerines facies) were deposited.

The phosphorites of the Northern Basins are low in P_2O_5 (<20%), fine-grained, compact, and glauconite-rich. They normally comprise two phosphatic units separated by a thin marl (Zaïer 1999), characteristically a nummulitic limestone bed.

Sekarna lies in a zone of Tertiary grabens (Graben Zone) that is bordered on the northwest by a zone of structural domes (Diapir Zone) and on the southeast by the Central Tunisian carbonate platform. Jebel (Mountain) Sekarna trends NW–SE and lies east of the Rohia graben (Fig. 3a), midway between Jebel Serdj and Jebel Ajred. Jebel Sekarna was affected by two systems of faults, the relative age of which is difficult to determine with certainty. It is generally believed that NNW/SSE-oriented faulting preceded NNE–SSW faulting. The geometry of the Sekarna deposit was controlled by closely spaced syn-sedimentary fault systems that developed during NW–SE extension. These faults strike NNW–SSE, NW–SE, or NNE–SSW and dip 40–60° to the W and NW. They appear mostly in the northern and western parts of the study area and were responsible for lateral facies variations and thickness variations in the host sedimentary rocks. The mineralized fault zones at Sekarna have approximately the same strike as the nearby Rohia graben (Fig. 3b).

The Sekarna area is underlain mainly by marine sedimentary rocks of Early Cretaceous to Eocene age (Fig. 4). Zaïer (1999) subdivided these rocks into five formations and suggested that the Zn–Pb–(Ba) mineralization formed during diagenesis of some phosphorite zones (Fig. 5). The Aleg Formation (Early Senonian) is a thick argillaceous marl with limestone intercalations; it is a distinctive lithology that outcrops over wide areas and grades upward into the Abiod Formation (Late Senonian), an intensely fractured gray micritic limestone (30–50 m) with planktonic foraminfera and cherty lenses and nodules in its uppermost parts. At other localities, the Abiod Formation contains upper and lower carbonate members; it is uncertain which member is represented at Sekarna.

The El Haria Formation (Paleocene) is too thin (2 m thick) to be shown on the map (Fig. 3b). It comprises black marls (illite–smectite mixed layers with minor kaolinite at the base and pure smectite at the top) with disseminated pyrite and glauconite, which implies marine regression and a suboxic–anoxic environment of deposition. This unit overlies the hard ground of the Abiod Formation and is overlain by transgressive conglomeratic phosphorites of the lower Metlaoui Formation.

The phosphorite, which is contained within the Metlaoui Formation, is more lithologically diverse at Sekarna than elsewhere in Tunisia (Gafsa Basin and Eastern and Northern Basins) where it is hard, glauconite-rich, and well-silicified. The sequence consists of graded phosphatic–glauconitic microconglomerate beds (unit A) overlain by a thick well-bedded Early Eocene carbonate series with abundant nummulites (units B and C).

Unit A is the richest in phosphorite and corresponds to the "Série Phosphatée." It is a green to brown gray phosphatic–

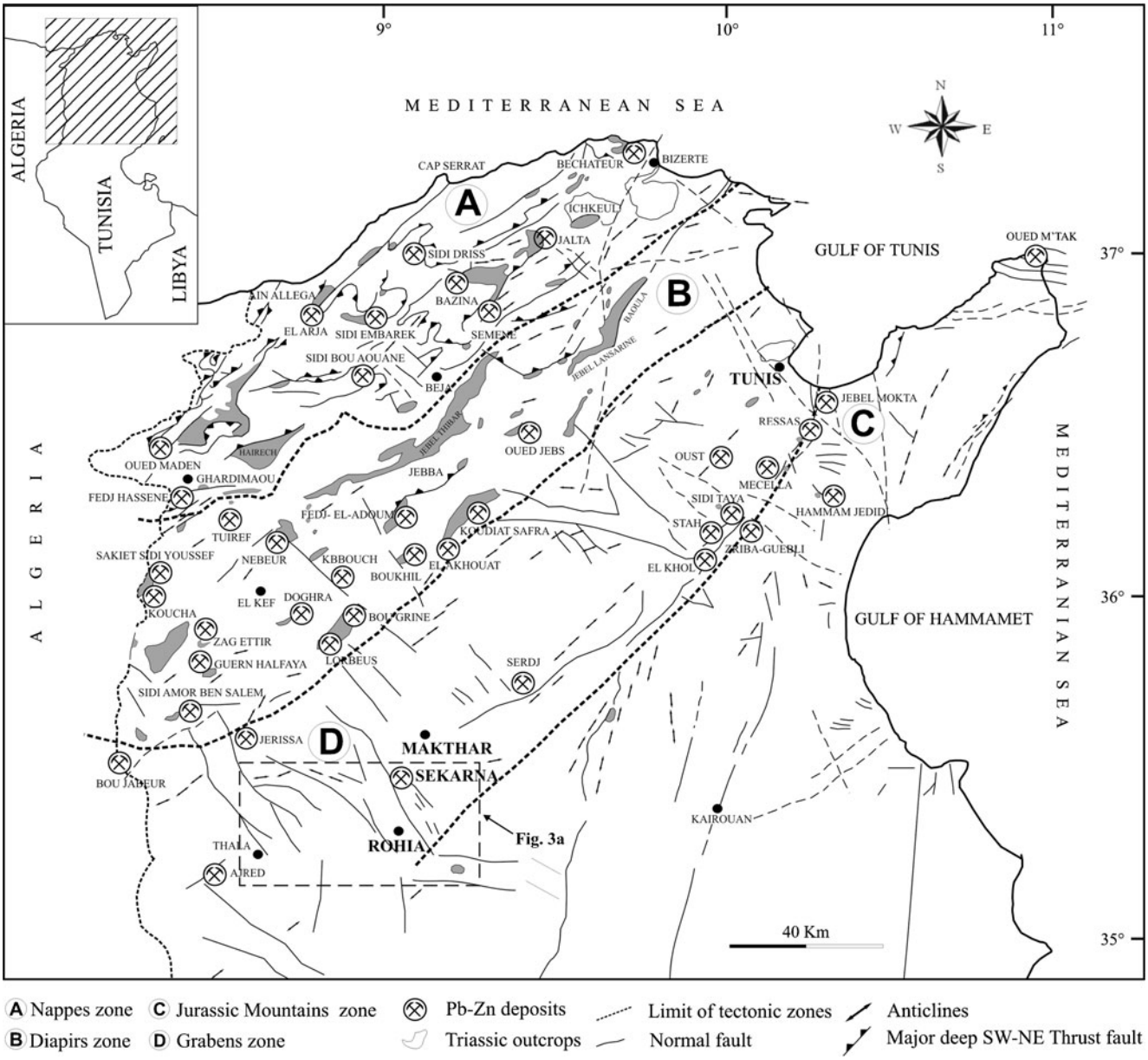

Fig. 1 Map showing the location of the study area within the main tectono-sedimentary units of Tunisia and the locations of the major ore deposits (modified from Bouhlel 1993; Bouhlel et al. 2007; Perthuisot et al. 1987; Sainfeld 1952)

glauconitic microconglomerate that outcrops as massive layers (20–80 cm) with total thicknesses of 5 m (Saint Pierre) to 7 m (Ras El Guézir). The absence of open-marine fossils and the abundance of clayey mud–wackstones suggest that the unit was deposited in restricted, poorly oxygenated deep water, presumably during a transgression.

Unit B is the thickest member (20 m) of the Metlaoui Formation. Carbonate rocks with a conglomeratic appearance ("calcaires en boules") alternate with dolomitic interbeds. Unit C has at its base a 4- to 5-m-thick dark gray fine dolomite with sporadic nummulites. These rocks are overlain by 8–10 m of micritic limestone with nummulites. The Metlaoui Formation is overlain by the Souar Formation, a thick sequence dominated by marls of Late Eocene age. Sedimentary strata show facies changes and thickness changes over short distances. This is thought to reflect syn-sedimentary faulting during Maastrichtian–Ypresian tectonic and/or halokinetic events.

Analytical methods

Representative samples of mineralized and non-mineralized rocks were obtained from the Saint Pierre and Saint Eugène mines. All were examined by X-ray diffraction and transmitted and reflected light microscopy. Bulk rock chemical

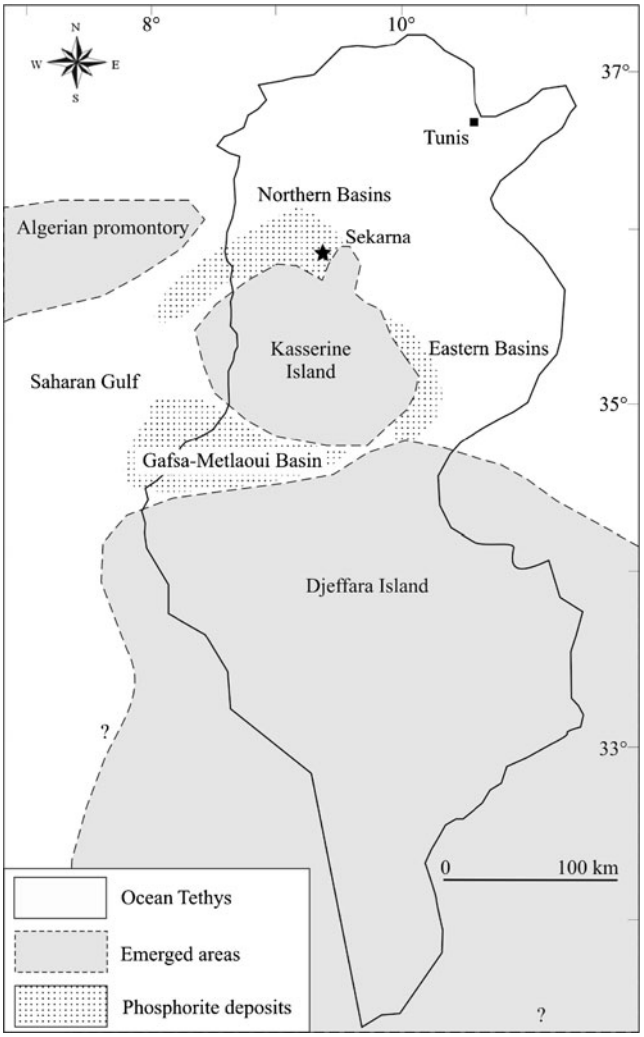

Fig. 2 Palaeogeographic setting of Tunisia during the Early Eocene showing the location of the study area (modified from Sassi 1974; Winnock 1980; Zaïer et al. 1998)

analyses of six phosphorite samples were performed at ActLabs (Ontario, Canada) using the 4LITHO, 4B-INNA, and 4B1 packages. Method descriptions can be found at http://www.actlabs.com.

Trace elements in sphalerite and galena were analyzed at the Department of Earth Sciences, Università della Calabria, Italy, by laser ablation–inductively coupled plasma mass spectrometry (LA-ICP-MS) using an Elan DRCe (Perkin Elmer/SCIEX) connected to a New Wave UP213 Nd-YAG laser (213 nm). Ablation craters were 50 and 80 μm in diameter and were analyzed with a frequency of 10 Hz and effluence of about 20 J/cm^2. Trace and rare earth element (REE) concentrations could be analyzed down to the parts per billion levels. External calibration was performed using the NIST SRM 612 glass standard in conjunction with Zn and Pb concentrations that had been determined independently by SEM-EDS. Calibrations were regularly checked during analytical sessions using the BCR2 glass reference material. Raw data were processed using the GLITTER program (Barca et al. 2007).

Fluid inclusions in Saint Pierre sphalerite was examined in 20 doubly polished sections. The microthermometry was performed on ~200-μm-thick wafers using a Linkam THMS-600 Heating Freezing stage. The stage was calibrated between −180°C and 600°C by measuring phase changes in fluid inclusions of known composition. Measurement error was ±2°C for homogenization temperatures and ±0.2°C for melting temperatures. Salinities were determined from the last melting temperature of ice using the equation of Bodnar (1993) for the H_2O–NaCl system. Liquid/vapor phase ratios were estimated using standardized charts (e.g., Shepherd et al. 1985) with an error of ±10 vol.%.

Sulfur isotope compositions were determined for 22 sulfide and sulfate samples at the US Geological Survey in Denver by the continuous flow method (Giesemann et al. 1994) using a ThermoFinnigan Delta mass spectrometer. Reproducibility was ±0.2‰. The data are reported as per mil deviations from the Vienna Cañon Diablo Troilite (VCDT) standard. Carbon and oxygen isotope compositions were determined by the phosphoric acid method (McCrea 1950). Mass spectrometry was carried out using a Finnigan MAT 252. The results are reported as per mil deviations from the Vienna Pee Dee Belemnite (VPDB) and Vienna Standard Mean Ocean Water (VSMOW) standards, respectively. Reproducibility was better than ±0.2‰ (1σ) for both $\delta^{13}C$ and $\delta^{18}O$.

For lead isotopic compositions, galena was separated by careful handpicking under a binocular microscope and then rinsed with doubly distilled water. Aliquots weighing about 1 mg were analyzed by thermal ionization mass spectrometry at the Geochronology and Isotope Geochemistry Laboratory, University of North Carolina, Chapel Hill, following the procedure described by Skaggs (2010).

Host rock petrography and geochemistry

Petrography

The ore-hosting phosphorite is similar to other Tunisian Late Paleocene–Early Eocene phosphorites (Sassi 1974; Chaabani 1995; Béji-Sassi 1999; Zaïer 1999). The rock fabrics and lithostratigraphic position are consistent with a commonly invoked model that involves authigenic mineral growth in fine-grained marine sediments located at the oxic–suboxic interface in nearshore depositional environments (Baturin 1982; Brunett et al. 1983; Froelich et al. 1988; Föllmi 1990; Jarvis 1992; Krajewski et al. 1994).

The phosphorites are granular and include authigenic phosphatic grains (pellets, coprolites, phosphatized fossils); biogenic grains (fossil teeth, skeletal fragments); non-

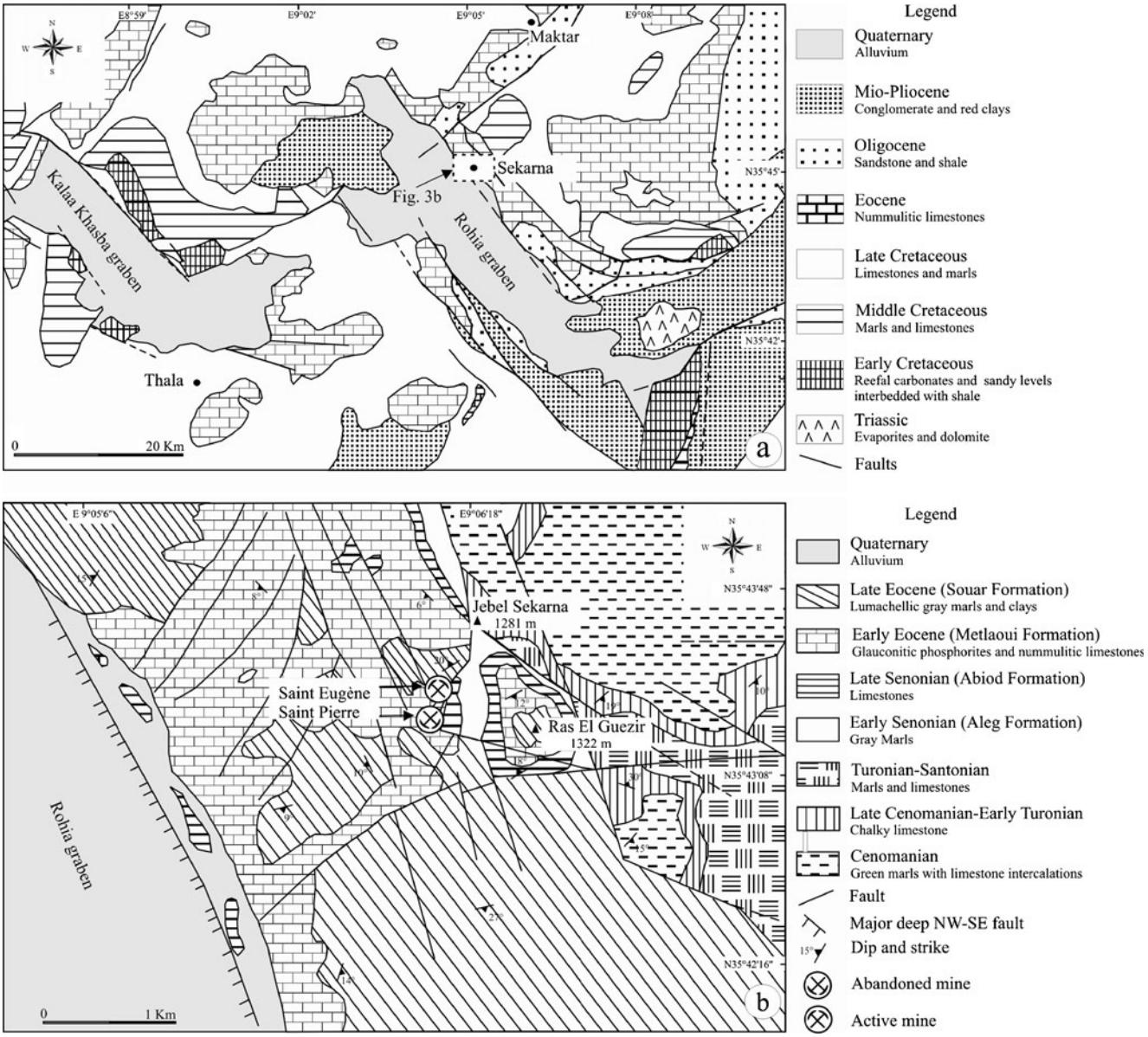

Fig. 3 **a** Regional geological map showing the Rohia graben (modified from Jauzein 1967). **b** Geological map of the study area showing the location of the main deposits (modified from Zaïer 1999)

phosphatic grains (quartz, glauconite, lithoclast, microcrystalline carbonate aggregates); and cement (carbonates, silicates) with packstone to grainstone textures. The phosphatic grains are dominated by carbonate fluorapatite (CFA). The clay fraction of the phosphorite, which reaches 1–5%, is composed of kaolinite, glauconite, and minor illite.

Carbonates dominate the cement in non-mineralized phosphorite. In contrast, mineralized rocks are depleted in carbonate and enriched in silica. Silicified rocks are characterized by euhedral quartz, particularly in mineralized areas, which occurs as replacements of carbonate cement and as inclusions within sphalerite and barite. Quartz in some samples shows growth layers and birefringent inclusions of anhydrite. Unlike phosphorite and glauconite grains, which show sutured flat grain shapes, concavo-convex contacts, and other textural signs of compaction, the euhedral quartz grains are undeformed, displaying euhedral shapes and lacking strained extinction. This implies that silicification postdated compaction. Silicification was commonly intense, filling open spaces and locally replacing the carbonate cement with euhedral quartz crystals with straight intercrystalline boundaries.

Silicification appears from textural observations to have occurred relatively late in the diagenetic history of the phosphorites. It is linked to the base metal sulfide mineralization, but likely represents a pre-mineralization stage.

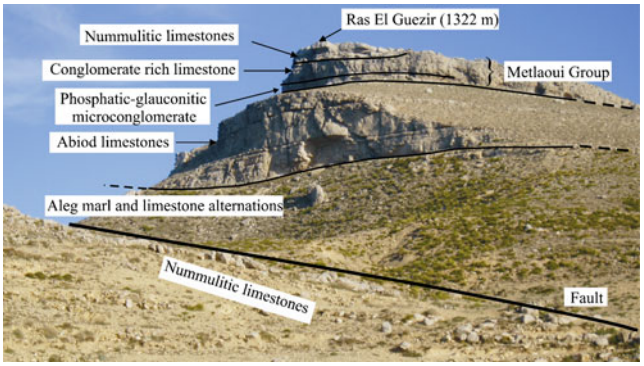

Fig. 4 Outcrops of Late Cretaceous–Early Eocene sedimentary sequences in Ras El Guezir (1,322 m), 800 m from the Saint Pierre deposit. The microconglomeratic phosphorite lies between reduced marls (~1.5 m thick) of El Haria Formation and the upper carbonate (~30 m thick) of Metlaoui Formation

Geochemistry

Whole-rock chemical analyses (Table 1) show that mineralized rocks are dominated by SiO_2 (30.3–39.8%), CaO, and P_2O_5, with all other oxides (MnO, MgO, Na_2O, K_2O, TiO_2) below about 1%. Non-mineralized samples exhibit higher CaO (38.1–42.3%) and MgO (2.4–5.1%). P_2O_5 ranges from 19.1% to 23.7% and is slightly higher in non-mineralized samples. Al_2O_3, TiO_2, and K_2O are indistinguishable between mineralized and non-mineralized rocks, reflecting relatively uniform contributions of detrital material.

Zn, Pb, and Ba in mineralized samples (n=2) average 3,315, 1,520, and 4,269 ppm, respectively. The highest grade samples contained 5.3% Zn and 2.6% Pb. Minor to trace As, Ag, and Sb substitute for Pb in the galena lattice, and Cd substitutes for Zn, giving rise to relatively high concentrations of these elements in mineralized samples. Similarly, Sr substitution in the barite lattice explains the elevated Sr in mineralized samples. Non-mineralized phosphorites have higher Ni and Mo (70–90 and 11–31 ppm, respectively) than mineralized samples (20–30 and 11–16 ppm, respectively). Ni and Mo are positively correlated with P_2O_5 and Na_2O, which indicates that these metals are related to CFA minerals.

Compared with phosphorite from the Gafsa–Metlaoui Basin (sample KEC1), non-mineralized phosphorite at Sekarna is slightly enriched in V, Ba, Ni, Mo, U, and ∑REE and is depleted in Sr, Zn, and Cd. Variations in the trace elements of phosphorite in the two localities can be attributed either to varying depositional conditions (basin configuration, redox conditions, productivity) or mixing of chemical precipitates and detritus shed from chemically distinct source areas.

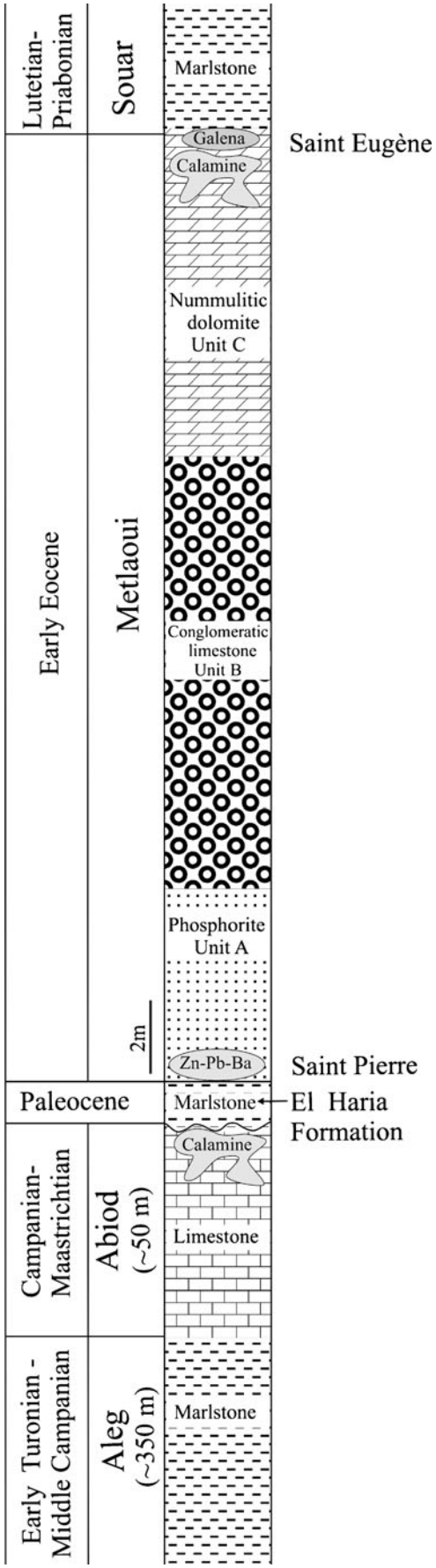

Fig. 5 Simplified composite lithostratigraphic column for the Sekarna area showing the stratigraphic position of the major sulfide and non-sulfide deposits

∑REE and Y contents of the samples average 741.5 and 295 ppm, respectively, higher than average phosphorite (462 ppm REE, 275 ppm Y; Altschuler 1980). PAAS-normalized (McLennan 1989) REE patterns display a slight enrichment in heavy REE (HREE), with $(La/Yb)_N$ of 0.85–0.94 and $(La/Sm)_N$ of 0.69–0.86. All samples have high $(La/Yb)_N$ ratios relative to modern seawater (0.2–0.5; Reynard et al. 1999), probably reflecting adsorption onto the apatite lattice during early diagenesis. The yttrium anomaly in our samples varies from 1.54 to 1.66, and the La/Nd ratio varies from 0.99 to 1.19, which is indistinguishable from seawater (Shields and Stille 2001).

Sulfide minerals are very low in ∑REE (<3 ppm) compared with CFA, so their contribution to whole-rock REE content is negligible. The good correlation between P_2O_5 and ∑REE (R^2=0.72) suggests that the REE inventory of the rocks is controlled by the phosphate components. Non-mineralized and mineralized phosphorites display similar REE patterns (Fig. 6); both resemble seawater, with negative Ce anomalies and flat or slight enrichment in HREE enrichment. It would appear that both phosphorite types obtained REE from seawater and record depositional conditions similar to modern oxic–suboxic seawater.

The Sekarna patterns resemble patterns that have been reported for phosphorites elsewhere in Tunisia (Béji-Sassi 1999; Ounis et al. 2008) as well as phosphorites of Mesozoic and Cenozoic age elsewhere in the Tethyan province (McArthur and Walsh 1984).

Mineralization

Saint Pierre deposit

Both hypogene and supergene Zn–Pb deposits occur in Sekarna area. The Saint Pierre deposit is a hypogene stratiform Zn–Pb–(Ba) sulfide deposit (10–13% Zn, 3–5% Pb) that is hosted by unusually hard, massive, dark gray, phosphatic–glauconitic microconglomerate of Ypresian age (Fig. 7a). Additional massive galena (3–14%) and supergene non-sulfide Zn minerals, such as Fe-poor smithsonite (<2 wt.% FeO), hemimorphite, and hydrozincite, occur in the Late Cretaceous carbonate rocks in karstic cavities along N20°–N40° trending faults. The mineralized unit is underlain by Paleocene marls and overlain by Nummlitic limestones. The mineralization appears to fill a stratiform lens-shaped structure concordant to bedding and trending WNW to NW. The mineralized zones are associated with major faults that are interpreted to have been feeder channels for hydrothermal fluids. The mineralization extends 200–300 m along strike and 100 m across strike. The sulfides do not appear to have formed by filling open space in fractures. It is likely that the mineralization was emplaced after the most significant folding and faulting events that affected the area. Mineralization is texturally and mineralogically simple, comprising sphalerite (90% of the ore), galena, Fe sulfides, and barite, and was preceded by a silicification of the host rock carbonate. Sphalerite and galena occur as cements around phosphatic pellets, glauconite, and detrital or euhedral quartz (Fig. 8a–d).

The ore-stage sulfides formed after burial diagenesis by the dissolution and replacement of either the rock matrix or earlier carbonate cements. Sulfide textures clearly indicate that the minerals grew during the late diagenetic to epigenetic stages in the evolution of the host sequence. Barite, which averages ~5.76% Sr, is a minor constituent of silicified phosphatic marls where it occurs as fibroradiated concretions. The concretions are up to 3 cm in diameter, spherical to ellipsoidal in shape, radial in structure, and are composed of elongate barite prisms and fibers. Barite is intergrown with phosphorite grains, euhedral quartz, and glauconite. Barite also fills intergranular space and microfractures in some phosphatic grains and occurs as micrometer inclusions in sphalerite (Fig. 8e, f).

Sphalerite, the major ore sulfide, occurs as disseminated grains or massive aggregates that are typically reddish brown to yellow, anhedral to subhedral, and medium-grained (1–10 mm). In transmitted light, some sphalerite crystals are finely zoned, showing alternating reddish and yellow zones and distinct growth layers. Galena occurs as large (>2 cm), well-formed crystals in simple cubic forms and, like sphalerite, as dendritic intergrowths. Galena appears to have formed late in the paragenetic sequence as it commonly cements other sulfides. Massive galena occurs with calamine in the Abiod and Upper Metlaoui carbonate rocks. Colloform cerussite and anglesite are intergrown within fractures in galena and along grain boundaries.

Iron sulfides occur as minor disseminations in all paragenetic stages. Pyrite formed early in the paragenesis (diagenetic pyrite), whereas later paragenetic stages are characterized by mixed marcasite and pyrite. The earliest pyrite typically occurs as framboids or micron-sized euhedral crystals disseminated in the argillaceous matrix or between larger mineral grains. Pyrite also occurs as rims and as replacements of glauconitic and phosphatic pellets, foraminifers, and gastropods. The upper part of the Saint Pierre ore body is oxidized and contains supergene minerals, including Cd-rich smithsonite, Zn silicates, Fe oxyhydroxides, and minor Pb minerals.

Saint Eugène deposit

Saint Eugène is a non-sulfide Zn–Pb deposit (35–40% Zn). The ore bodies are hosted by dolomitic limestone and are associated with two major NE/SW-trending faults. The main Zn mineral is smithsonite. Hemimorphite, hydrozincite,

Table 1 Major (%) and trace element (in parts per million) contents of representative phosphorite samples

Sample	SEK1 NMP	SEK3 NMP	SEK4 NMP	SEK5 MP	SEK2 MP	KEC1 GM
SiO_2 (%)	18.20	22.45	9.31	30.38	39.88	6.97
Al_2O_3	1.22	1.21	0.88	1.51	1.47	1.28
Fe_2O_3(T)	2.17	1.99	1.69	1.75	1.68	0.56
MnO	0.03	0.02	0.02	0.002	0.003	0.003
MgO	3.88	2.43	5.12	0.37	0.42	0.62
CaO	38.76	38.18	42.35	32.61	28.05	45.88
Na_2O	0.41	0.48	0.42	0.42	0.38	1.42
K_2O	0.50	0.45	0.39	0.61	0.54	0.32
TiO_2	0.04	0.05	0.04	0.07	0.07	0.053
P_2O_5	19.73	23.77	19.14	23.66	20.15	27.81
LOI	13.74	9.06	19.02	5.60	4.90	11.9
Total	98.67	100.10	98.38	96.99	97.56	96.81
V (ppm)	254	164	183	297	275	52
Ba	45	99	89	4,563	3,975	40
Sr	539	573	693	851	785	1,816
Y	299	316	251	326	284	140
Zr	34	41	28	41	41	44
Cr	297	305	287	482	437	273
Ni	64	85	58	31	21	22
Cu	15	16	13	21	34	11
Zn	84	33	13	3,400	3,230	290
Cd	5.6	2.9	0.8	349	302	60.8
As	18.7	37.2	37.6	68.2	107	6.5
Rb	12	11	9	15	13	6
Nb	1	2	1	3	3	2
Mo	11	31	25	16	16	11
Ag	<0.3	1.1	0.8	2	2	0.9
Sb	2.8	4.9	5.4	8	45.3	1
Pb	31	376	207	1,270	1,770	5
Th	9.3	9.7	5.5	7.5	6.8	14.1
U	36.2	55	47.8	67.3	57.2	34.2
La	184	186	155	197	166	108
Ce	195	213	152	223	182	164
Pr	38.90	41.90	30.50	45	38.20	23.5
Nd	167	182	130	197	167	96.5
Sm	34.70	37.60	26.20	41.40	35	18.9
Eu	8.26	9	6.41	9.93	8.32	4.34
Gd	37	40.10	29	43.50	36.50	18.4
Tb	5.60	6	4.40	6.40	5.50	2.8
Dy	32.50	34.50	25.50	36.60	31	16.1
Ho	7.10	7.50	5.70	7.80	6.60	3.5
Er	19.60	20.80	15.90	20.80	17.90	10.1
Tm	2.56	2.67	2.09	2.64	2.26	1.38
Yb	15.80	16.10	12.80	15.40	13.10	9.2
Lu	2.39	2.46	2	2.28	1.98	1.46
∑ REE	750.41	799.63	597.50	848.75	711.36	478.18
Ce/Ce*	0.50	0.53	0.48	0.52	0.50	0.73
Eu/Eu*	2.03	2.12	1.79	2.24	2.05	1.48
$(La/Sm)_N$	0.77	0.72	0.86	0.69	0.69	0.83
$(La/Yb)_N$	0.86	0.85	0.89	0.94	0.94	0.87
$(Dy/Yb)_N$	1.24	1.29	1.20	1.43	1.43	1.05
Y ano	1.57	1.57	1.66	1.54	1.58	1.49
La/Nd	1.10	1.02	1.19	1.00	0.99	1.12

LOI loss on ignition, *NMP* non-mineralized phosphorite, *MP* mineralized phosphorite, *GM* Gafsa–Metlaoui phosphorite

$Ce/Ce^* = 3Ce_N/(2La_N + Nd_N)$ (The subscript N refers to normalization of concentrations against the PAAS values)

$Eu/Eu^* = Eu_N/(Sm_N + Gd_N)^{0.5}$

cerussite, and anglesite are minor constituents of the deposit (Fig. 7b). Calcite is often associated with smithsonite. Fe oxyhydroxides are also very common.

Smithsonite $\delta^{18}O$ and $\delta^{13}C$ values are −5.1‰ and 28.3‰, respectively. Dolomitic host rocks show a relatively narrow range of $\delta^{18}O$ (21.6–23.9‰), and a wider range of $\delta^{13}C$ (−2.3‰ to 2.6‰, Table 2). The dolomite $\delta^{13}C$ values suggest that carbon was derived from both dissolution of the precursor limestones and oxidation of organic carbon.

The oxygen isotopic compositions of Sekarna smithsonites are similar to the compositions that have been reported for other supergene smithsonites elsewhere in the world (Boni et al. 2003; Coppola et al. 2008, 2009; Gilg et al. 2008). Both the mineral assemblage (Fe-poor smithsonite, Fe oxyhydroxides, Pb sulfate carbonates) and the C–O isotopic signature are typical of ores of supergene origin (Gilg and Boni 2004a, b; Gilg et al. 2008). The fact that dolomite $\delta^{18}O$ values are about 4‰ lower than the smithsonite values is in accord with the model of isotope fractionation between carbonate minerals and water proposed by Gilg et al. (2008). The fluid that oxidized the precursor sulfides at Saint Eugène was likely of meteoric origin. Carbonate block faulting during the late stages of the Early Tertiary Alpine orogeny could have enhanced deep circulation of meteoric fluids and the oxidation of primary sulfides.

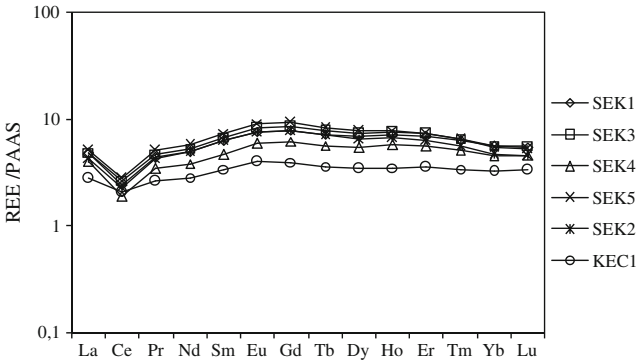

Fig. 6 PAAS-normalized REE patterns of mineralized and non-mineralized phosphorites. PAAS composition after McLennan (1989)

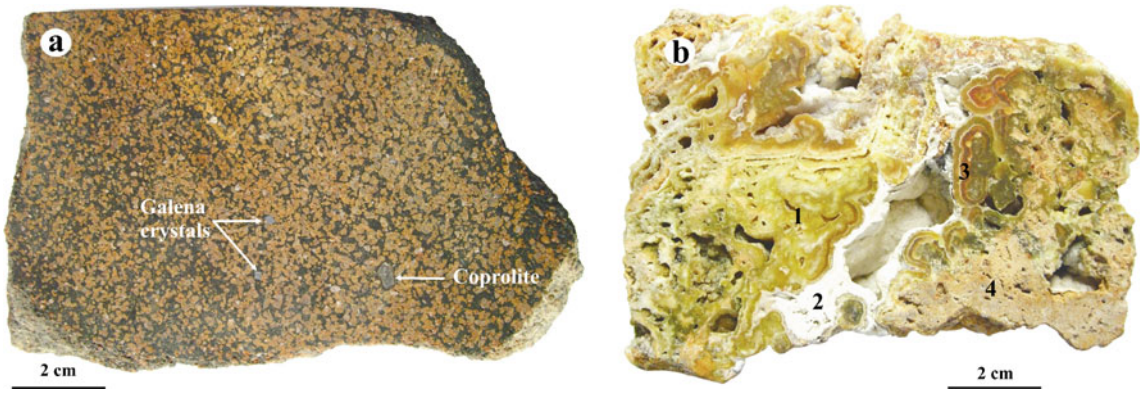

Fig. 7 **a** Typical ore sample from Saint Pierre. Fine-grained sphalerite (*reddish* to *yellow*) has replaced carbonate cement in Eocene phosphorite (*dark color*). **b** Typical ore sample from Saint Eugène concretionary, colloform calamine ore in karstic cavities within Early Eocene limestone. *1* Greenish to yellow colloform and concretionary smithsonite. *2* White colloform hydrozincite. *3* Fe oxides with Fe-rich smithsonite. *4* Weathered carbonate host rock

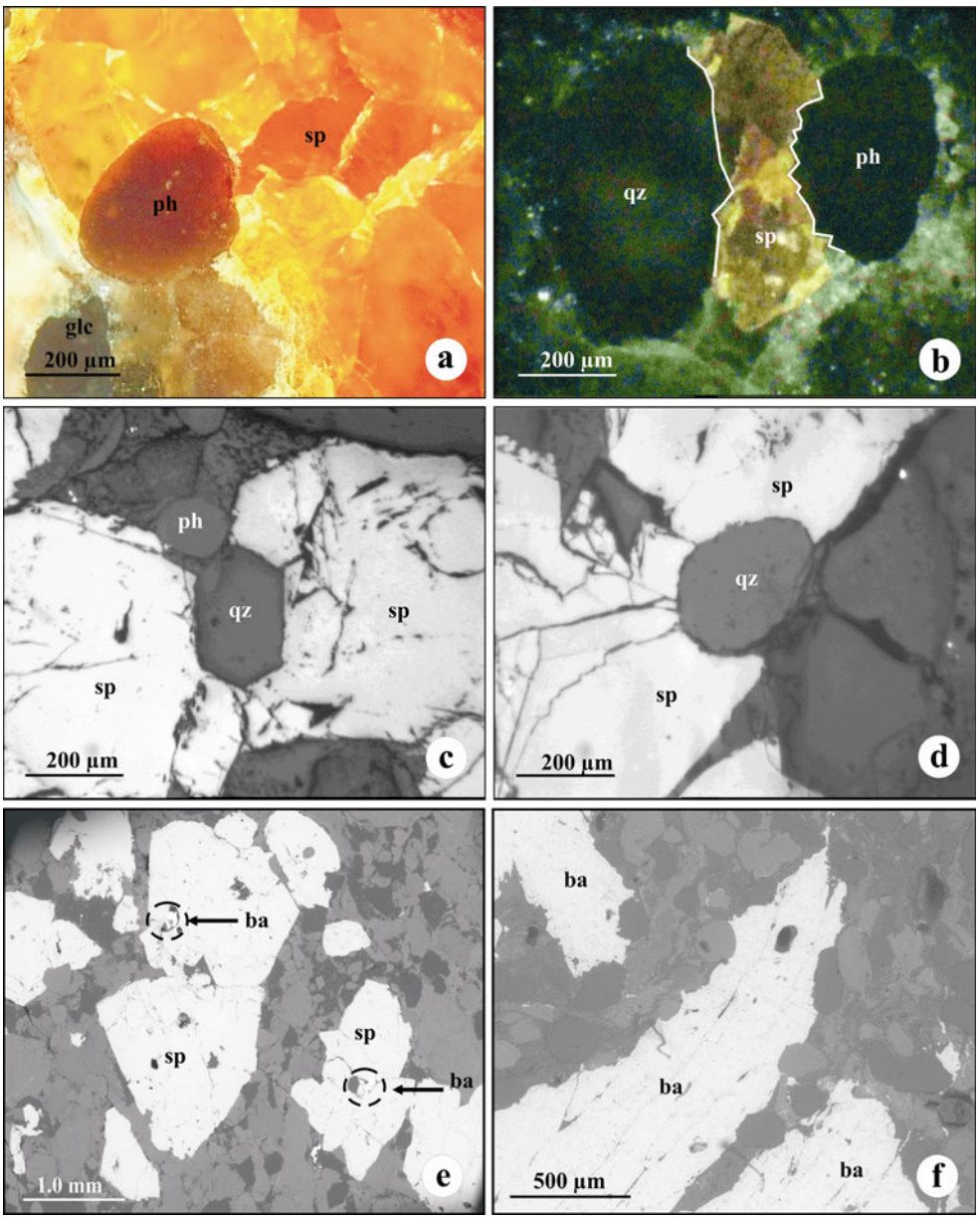

Fig. 8 **a**–**d** Photomicrographs of polished sections illustrating sulfide–host rock textures. **a** Polarized reflected light photomicrograph showing yellow red sphalerite (*sp*) cementing phosphatic pellets (*ph*). **b** Polarized reflected light photomicrograph showing sphalerite infilling between phosphatic pellet and detrital quartz (*qz*). Note the tangential and sutured contacts between sphalerite, detrital quartz, and phosphorite grains, indicative of intergranular pressure. **c** Sphalerite cementing euhedral quartz and phosphorite grains. **d** Sphalerite surrounding detrital quartz. **e**, **f** Backscattered electron images showing the relationship between barite and the surrounding minerals. **e** Barite inclusions (*white spots*) in sphalerite in a matrix of francolite. Francolite contains up to 1.8 at.% Na and up to 4.6 at.% F. Cd in sphalerite is up to 0.8 at.% (equivalent to 1.9 w.t% Cd). **f** Fibrous barite replacing carbonate cement and showing irregular outlines with rounded to sub-rounded grains

During this period, several short-lasting emersions and intense weathering episodes facilitated karst formation in the Late Cretaceous and Early Eocene carbonate rocks and oxidation of sulfide bodies by downward-percolating meteoric waters.

Geochemistry

Trace elements

Data from nine polished sections (Tables 3 and 4) indicate that Sekarna sphalerite is low in Fe (average 652 ppm) and high in Cd (average 11,337 ppm). Cadmium concentrations are variable, ranging from 5,789 to 20,106 ppm (Fig. 9). Within an individual hand specimen, Cd varies by as much as a factor of 3. Fe and Cu contents range from 344 to 1,312 ppm and from 25 to 1,207 ppm, respectively. Within had specimens, Fe and Cu vary by a factor of <3.

Sekarna sphalerite comprises a single generation that displays color-banded growth zones corresponding to oscillations in minor element concentrations. LA-ICP-MS step traverses show that light yellow zones in crystal cores are lower in Cu and higher in Cd and Fe than reddish brown zones in crystal rims. The increase in Cu toward crystal rims may reflect the introduction of Cu-rich fluids.

Neither Cu- nor Cd-bearing minerals were present as inclusions in sphalerite; thus, these two elements would appear to be in solid solution in the sphalerite lattice. In contrast, submicroscopic pyrite was identified in some sphalerites. Strong correlations in spot analyses between As and Pb, As and Sb, and Pb and Sb (R^2=0.6) could reflect submicroscopic inclusions of galena and/or tetrahedrite.

Trace elements in Sekarna galena are predominantly As, Ag, Cd, and Sb. Sb ranges up to 1,740 ppm and Ag from 4 to 122 ppm. Cd is higher than in most Mississippi Valley-type (MVT) deposits (Hall and Heyl 1968; Hagni 1983; Song 1984).

Elevated Fe, Cu, and Zn in galena were almost certainly due to the ablation of microscopic inclusions of pyrite, chalcopyrite, and sphalerite. Strong correlations between As and Cd (R^2 above 0.8) suggest that these elements are probably associated with inclusions of minerals such as sphalerite.

Fluid inclusions

Fluid inclusions in Saint Pierre sphalerite are 20–80 μm in diameter. According to their appearance at room temperature, two types of inclusions were recognized: single-phase liquid aqueous inclusions (L) that are abundant and generally smaller than 20 μm and two-phase inclusions (L+V) that are located along the growth zones and are about 90% liquid. Inclusion appearance is highly variable and can be characterized as irregular, slightly rounded and flattened, tubular, or spheroidal/oblate.

Homogenization temperatures (T_H) were determined principally on two-phase liquid-rich inclusions, which were relatively large and regular in shape. These inclusions showed no textural evidence of necking down and are interpreted to be primary.

Microthermometric results ranged from 80°C to 130°C. First ice melting temperatures ranged from −59°C to −34°C. These temperatures, which are lower than the eutectic temperature in the NaCl–H_2O system (T_e=−21.2°C), indicate that the fluid is complex and may contain Ca^{2+} (H_2O–NaCl–$CaCl_2$: T_e≈−55°C) and/or Mg^{2+} (H_2O-NaCl-$MgCl_2$: T_e≈ −35°C; Crawford 1981; Roedder 1984; Shepherd et al. 1985). Final ice melting temperatures ranged from −11°C to −22°C, which indicates a salinity range of 15–24 wt.% NaCl eq. The measured salinities are lower than the eutectic salinity for the binary system NaCl–H_2O (23.3 wt.% NaCl eq).

The fluid inclusion observations allowed two types of fluids to be identified in Sekarna sphalerite:

1. An H_2O–NaCl–$CaCl_2$, moderate temperature (110–130°C) and moderate salinity (~15 wt.% NaCl eq) fluid that is predominant in brown reddish zones of sphalerite
2. An H_2O–NaCl–$CaCl_2$, moderate- to low-temperature (80–110°C) and high-salinity (~24 wt.% NaCl eq) fluid that is associated mainly with light yellow crystal cores

The measured temperatures and calculated salinities lie within the ranges that have been reported for MVT deposits worldwide (50–250°C, 10–30 wt.% NaCl eq). The variations in salinity and eutectic temperature in primary two-phase fluid inclusions in zoned sphalerite could reflect mixing between two chemically distinct fluids or phase separation of a single fluid.

Table 2 Carbon and oxygen isotopic compositions of smithsonite and dolomite

Sample references	Composition	$\delta^{13}C_{VPDB}$ (‰)	$\delta^{18}O_{VSMOW}$ (‰)
SM1	Yellow colloform smithsonite from Saint Eugène	−5.1	28.3
SM2	Massive crystalline smithsonite from Saint Eugène	−5.2	28.3
D1	Early Eocene massive gray dolomite from Saint Eugène (unit C) hosted sample SM1	−2.3	23.9
D2	Early Eocene yellow dolomite from Saint Eugène (Unit C) hosted sample SM2	2.3	21.6
A1	Abiod dolomitized limestone from Saint Pierre	2.6	23.0

Table 3 LA-ICP-MS analyses of sphalerite from Saint Pierre

Sample references	Spot analyses	Description	Ti	Mn	Fe	Co	Cu	As	Ag	Cd	Sn	Sb	Pb
P-SP (disseminated sphalerite)	03-P-SP-01	Brown reddish sphalerite	5	nd	451	0.5	174	nd	572	5,789	0.1	1	28
	04-P-SP-02	Brown reddish sphalerite	4	nd	344	0.5	1,019	6	31	6,822	nd	3	20
	05-P-SP-03	Brown- reddish sphalerite	6	0.4	366	0.5	836	4	77	7,335	0.2	2	20
	06-P-SP-04	Light yellow sphalerite	7	0.2	480	0.3	593	46	4	11,705	0.1	51	63
	07-P-SP-05	Brown reddish sphalerite	3	nd	388	0.4	1207	72	6	6,528	nd	118	92
	08-P-SP-06	Light yellow sphalerite	3	0.2	461	0.3	227	41	4	14,230	0.1	26	33
	09-P-SP-07	Light yellow sphalerite	7	nd	531	0.3	51	2	nd	11,882	0.2	4	7
	10-P-SP-08	Light yellow sphalerite	nd	nd	419	0.5	215	21	3	12,654	nd	22	24
SP1 (disseminated sphalerite)	08-SP1-01	Light yellow sphalerite	2	0.2	676	0.4	765	70	10	16,001	1.4	144	129
	09-SP1-02	Brown reddish sphalerite	1	nd	662	0.7	368	41	8	10,347	2.0	72	40
	11-SP1-04	Light yellow sphalerite	nd	0.4	967	0.6	529	54	13	16,272	4.1	145	74
SP3 (massive sphalerite)	09-SP3-01	Light yellow sphalerite	2	nd	852	0.4	188	32	11	14,845	nd	68	46
	10-SP3-02	Brown reddish sphalerite	1	0.2	686	0.3	131	28	10	9,578	0.1	74	42
	11-SP3-03	Light yellow sphalerite	2	nd	571	0.3	398	21	6	12,399	nd	37	87
	13-SP3-05	Brown reddish sphalerite	2	0.3	628	0.3	415	49	13	11,844	0.1	75	109
SP4 (massive sphalerite)	21-SP4-01	Brown reddish sphalerite	nd	nd	600	0.5	774	57	7	9,158	2.7	38	69
	22-SP4-02	Light yellow sphalerite	2	0.1	596	0.4	820	50	7	10,120	0.1	94	97
SP-G4 (massive sphalerite)	19-SP-G4-01	Light yellow sphalerite	3	0.3	1,312	0.3	360	13	4	16,158	0.1	40	50
	20-SP-G4-02	Brown reddish sphalerite	2	0.1	914	0.4	422	11	4	10,243	0.1	61	37
SP-G5 (massive sphalerite)	15-SP-G5-01	Light yellow sphalerite	1	0.1	622	0.2	25	3	1	12,028	nd	9	34
	16-SP-G5-02	Brown reddish sphalerite	1	0.1	579	0.2	138	22	9	7,721	0.1	51	24
	17-SP-G5-04	Light yellow sphalerite	1	0.2	1,183	0.4	119	7	3	20,106	nd	26	16
	18-SP-G5-03	Brown reddish sphalerite	1	0.1	712	0.3	1,072	25	9	6,988	0.5	148	86

Trace element concentrations in parts per million

nd not detected

Sulfur isotopes

The sulfur isotopic compositions ($\delta^{34}S_{VCDT}$) of ore sulfides at Sekarna are relatively uniform with averages of −10.2‰ for sphalerite and −13.6‰ for galena (Table 5). Disseminated sphalerite is isotopically indistinguishable from massive sphalerite. Disseminated galena within phosphorite (−12.5‰, n=5) is slightly heavier than massive galena (−15.5‰, n=3) in the Late Metlaoui carbonate rocks (Fig. 10). Most of the $\delta^{34}S$ results for sulfate minerals (barite, celestite, and gypsum) range from 17.7‰ to 24.9‰, values that are similar to marine sulfates (e.g., Claypool et al. 1980).

Lead isotope compositions

The Pb isotope results for seven Sekarna galenas are compared in Fig. 11 with the Pb isotopic compositions of the major Pb–Zn Tunisian deposits (Bougrine, Fedj El Adoum, and Boujabeur) as well as the Pb isotope evolution curves of Zartman and Doe (1981). $^{206}Pb/^{204}Pb$ ranges from 18.7418 to 18.8627, $^{207}Pb/^{204}Pb$ from 15.6488 to 15.7902, and $^{208}Pb/^{204}Pb$ from 38.7976 to 39.27. Sekarna galena is isotopically homogenous, plotting in narrow fields that imply an upper crustal Pb source.

The Pb isotopic compositions of the major Tunisian ore deposits do not show a trend representing enrichment in radiogenic lead. There is no systematic relationship between Pb isotopes and geographic location, nor is there a relationship between Pb isotopes and age of wall rocks or deposit type. All the galenas plot along the upper crustal trend. The isotopic uniformity indicates a Pb source that was well-homogenized (Table 6).

Discussion

Diagenetic vs. epigenetic origin

At Saint Pierre, the Zn–Pb–(Ba) mineralized zone occurs within the lower Metlaoui organic-rich unit. The deposit was emplaced in an extensional zone at the edge of the Rohia Graben, the boundary fault of which has the same strike as the mineralized fault zones at Sekarna. The mineralized zone corresponds to a local depocenter immediately adjacent to faults that provided conduits for the ore fluids.

Table 4 LA-ICP-MS analyses of galena from Saint Pierre and Saint Eugène

Sample references	Spot analyses	Ti	Fe	Cu	Ni	Zn	As	Ag	Cd	Sb
P-G (disseminated galena in phosphorites from Saint Pierre)	03-P-G-01	0.5	nd	nd	nd	0.1	3.3	44	66	296
	04-P-G-02	0.7	nd	nd	0.1	0.7	0.9	105	28	239
	05-P-G-03	1.1	7.8	0.1	0.3	0.2	1.0	82	27	581
	06-P-G-04	0.7	nd	nd	0.1	nd	2.7	106	37	295
	07-P-G-05	1.5	5.1	0.5	0.2	4.5	0.4	105	29	451
	08-P-G-06	2.7	9.7	0.1	0.2	nd	nd	37	12	68
SP-G1 (massive galena in phosphorites from Saint Pierre)	03-SP-G1-01	nd	nd	1.1	nd	0.2	4.0	29	77	846
	04-SP-G1-02	0.9	nd	1.7	nd	nd	2.6	38	50	679
	05-SP-G1-03	0.2	nd	0.2	0.1	0.3	0.4	9	25	610
SP-G2 (massive galena in phosphorites from Saint Pierre)	06-SP-G2-01	0.7	nd	nd	nd	nd	0.5	5	21	239
	07-SP-G2-02	0.6	nd	0.1	nd	nd	5.7	8	88	233
	08-SP-G2-03	0.5	nd	nd	nd	0.2	5.5	6	82	237
	09-SP-G2-04	0.4	nd	nd	0.0	nd	1.9	8	42	219
	10-SP-G2-05	0.8	nd	nd	nd	nd	0.2	4	24	68
SP-G3 (massive galena from Saint Eugène)	11-SP-G3-01	1.0	nd	1.8	0.1	0.4	1.3	44	38	182
	12-SP-G3-02	0.8	nd	0.1	nd	nd	nd	38	23	84
	13-SP-G3-03	0.8	1.5	0.1	nd	0.2	nd	26	19	70
	14-SP-G3-04	0.2	0.9	1.1	0.1	0.1	6.8	64	108	263
G2 (massive galena from Saint Eugène)	10-G2-01	1.1	nd	0.8	nd	0.2	1.5	15	37	1,468
	12-G2-03	1.1	3.8	1.5	0.1	0.5	0.4	122	59	1,309
	14-G2-05	1.1	nd	0.1	nd	0.7	1.1	27	92	1,740
G3 (massive galena from Saint Eugène)	06-G3-01	0.3	nd	0.3	0.1	nd	3.1	28	92	363
	09-G3-04	1.3	nd	0.3	nd	nd	15.3	26	189	675

Trace element concentrations in ppm

nd not detected

The mineralization does not fill fractures but rather is lens-shaped and interstratified with phosphorite. The finely disseminated nature of the sulfides suggests that sulfide minerals were deposited where favorable horizons in the phosphorite were dissolved. The spatial correspondence of sulfide lenses and faults, the depositional temperatures ranging from 80°C to 130°C, and the homogeneous S and Pb isotopic compositions support a model in which fluids were expelled from a proximal depocenter by sediment compaction.

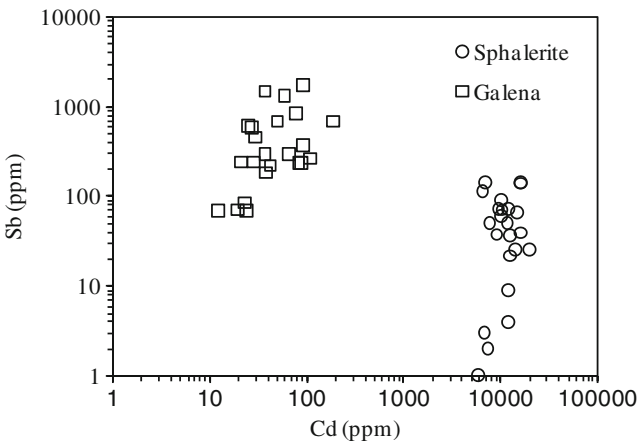

Fig. 9 Cd vs. Sb plot of laser ablation ICP-MS data for sphalerite and galena from Sekarna

The morphology, stratigraphic position, and geochemistry of REE, in particular of the phosphorites host rocks, are similar to the unmineralized CFA in other localities that formed during the diagenesis of organic-rich sediments. For this reason, the phosphorites are regarded as primary. The absence of diagenetic intergrowths of sphalerite or galena with phosphorite and glauconite suggests that sulfide deposition postdated diagenesis. Although carbonate cement is preserved in non-mineralized phosphorites, silicification and sulfide growth have destroyed sedimentary and earlier diagenetic textures within the ore zones. Sulfides did not replace phosphatic minerals; instead, sphalerite and galena formed as cements around phosphatic pellets, glauconite, and quartz (both detrital and euhedral). Taken together, these observations suggest a late diagenetic to epigenetic origin for the Zn–Pb mineralization.

Sphalerite in the Sekarna deposit is characteristically fine and reddish yellow in color with significant enrichment in Cd (average=11,337 ppm), some 21 to 74 times richer than sphalerite in other major MVT deposits in the world. High Cd, similar to Sekarna, is reported in a few MVT deposits,

Table 5 Sulfur isotopic compositions of sphalerite, galena, and barite from the Sekarna deposit and of celestite and gypsum from southern Tunisia

Sample references	Location	Composition	Mineralization type	$\delta^{34}S$ (‰)
SEKZn1	Saint Pierre	Sphalerite	Disseminated in phosphorites	−9.5
SEKZn2	Saint Pierre	Sphalerite	Disseminated in phosphorites	−9.3
P-SP/SP	Saint Pierre	Sphalerite	Disseminated in phosphorites	−10.8
SP1	Saint Pierre	Sphalerite	Disseminated in phosphorites	−10.1
SP2	Saint Pierre	Sphalerite	Disseminated in phosphorites	−10.3
SP3	Saint Pierre	Sphalerite	Disseminated in phosphorites	−10
SP4	Saint Pierre	Sphalerite	Disseminated in phosphorites	−10.8
SP5	Saint Pierre	Sphalerite	Massive ore	−11.2
SP6	Saint Pierre	Sphalerite	Massive ore	−10
SEKPb1	Saint Pierre	Galena	Disseminated in phosphorites	−12.8
SEKPb2	Saint Pierre	Galena	Disseminated in phosphorites	−12.9
GN1	Saint Pierre	Galena	Disseminated in phosphorites	−12.3
GN2	Saint Eugène	Galena	Massive ore in dolomite	−16
GN3	Saint Eugène	Galena	Massive ore in dolomite	−15.5
GN4	Saint Eugène	Galena	Massive ore in dolomite	−15.1
PG-G	Saint Pierre	Galena	Disseminated in phosphorites	−12.4
Ba1	Saint Pierre	Barite	Fibroradiated barite in phosphorites	25.3
Ba2	Saint Pierre	Barite	Fibroradiated barite in phosphorites	24.9
CMK1	Jebel Jebes (Eastern basins)	Nodular celestite	Celestite-bearing dolostone (El Haria Formation)	21.2
C-GAF	Jebel Chouabine (Gafsa–Metlaoui basin)	Celestite geode	Celestite-bearing evaporitic unit of Thelja member (Paleocene–Early Eocene)	22.5
G-CELS	Jebel Jebes (Eastern basins)	Gypsum	Early Eocene gypsum associated to nodular celestite (sample CMK1)	17.8
G-TH	Oued Thelja (Gafsa–Metlaoui Basin)	Gypsum	Eocene gypsum in massive gypsum deposit (Thelja member)	17.7
G-JJB	Jebel Jebes (Eastern basins)	Gypsum	Gypsum filling fractures in phosphorite beds	−9.5

including Kentucky–Tennessee (average=13,344 ppm; Jolly and Heyl 1968), Vazante (average=8,410 ppm; Monteiro et al. 2006), and the low-temperature Cd-rich zinc deposit of Niujiaotang, China (average=13,800 ppm; Liu et al. 1999); high Cd sphalerite is also known in phosphate-rich sediments (Nathan et al. 1996, 1997; Béji-Sassi and Sassi 1999).

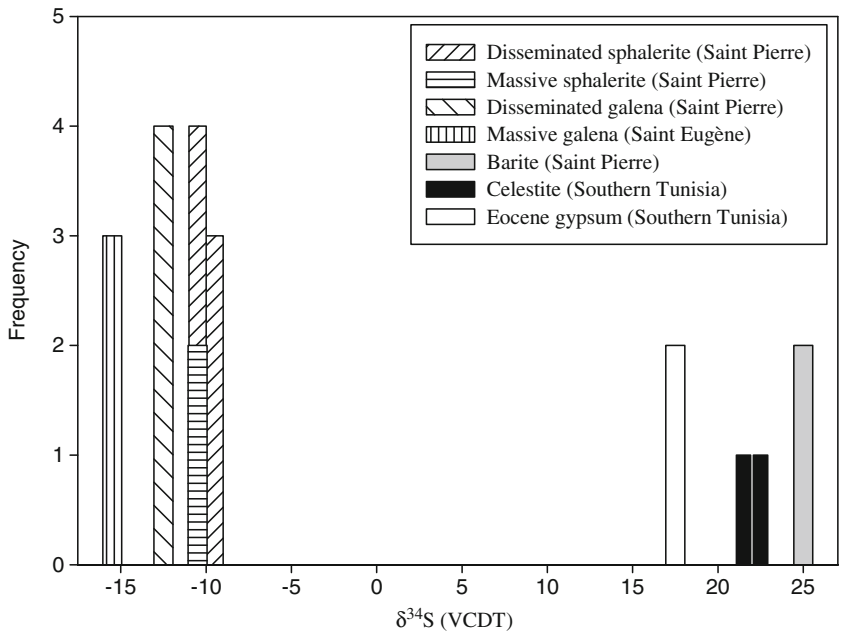

Fig. 10 Frequency distribution of S isotope values (per mil) for sphalerite, galena, and barite in the Sekarna deposit

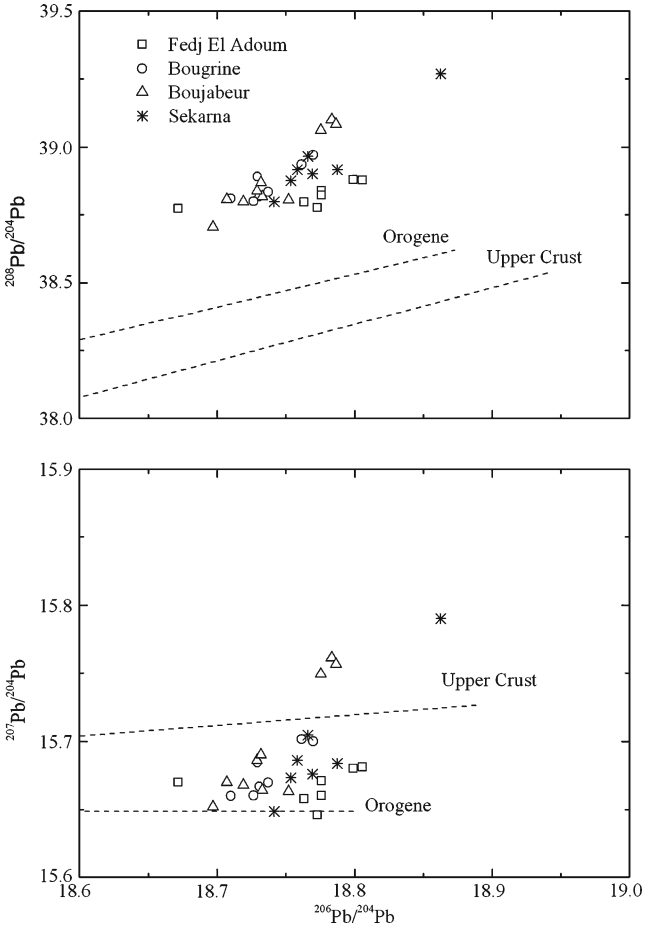

Fig. 11 Pb isotopic compositions of Sekarna galena plotted on $^{208}Pb/^{204}Pb$ vs. $^{206}Pb/^{204}Pb$ and $^{207}Pb/^{204}Pb$ vs. $^{206}Pb/^{204}Pb$ diagrams (after Zartman and Doe 1981). Pb isotopic compositions of galena from Fedj El Adoum, Bougrine and Boujabeur deposits are from Skaggs (2010)

The high Cd suggests that the hydrothermal fluid may have circulated through the underlying basin fill, which contains organic-rich sediments. Similarities in sphalerite composition between the Sekarna deposits and low-temperature deposits elsewhere, including the MVT deposits, may be explained by brines from similar sources traversing and leaching metals from sedimentary sequences.

The T_H and salinities of Sekarna sphalerite-hosted inclusions are consistent with an ore genesis model involving basinal brines like those that formed Tunisian MVT deposits (Bouhlel 2005) and MVT deposits in other areas of the world (Leach et al. 2005). The relatively uniform Pb isotopic compositions of Sekarna galena suggests a simple origin for the metals, namely, derivation from a single fluid generation that interacted with deep upper crust.

Diagenetic barite

Although sulfates (celestite, gypsum) have been described previously in phosphorites of Tunisia (Béji-Sassi 1999), Sekarna is the first reported occurrence of concretionary barite. Other stratigraphic intervals are known to contain abundant barite concretions, including mid-Cretaceous sediments, especially those of Albian age (France: Bréhéret and Brumsack 2000; Belgium: Dejonghe et al. 1987; Tunisia: Burollet et al. 1983), at the Cretaceous–Tertiary boundary (Soliman 1998; Ramkumar et al. 2005) and across the Paleocene–Eocene Thermal Maximum (PETM) period (Schmitz et al. 1997; Bains et al. 2000). Ba anomalies at the Cretaceous–Tertiary have been attributed to a detrital influx coincident with a fall in sea level (Ramkumar et al. 2005). Similar anomalies across the PETM were attributed to increased productivity (Bains et al. 2000).

The close association of celestite with evaporates is attributed to sulfate enrichment in evaporated pore waters or by the dissolution of evaporites, or else as a consequence of the transformation of aragonite to calcite and/or dolomite during early diagenesis (e.g., Yan and Carlson 2003). No evaporite sequences have been observed in Sekarna area, nor have evaporates been recognized in the sedimentary record at Sekarna. Thus, evaporation processes are unlikely to have been for the ultimate cause of celestite precipitation.

The sulfur isotopic compositions of celestite are consistent with literature data in showing a 5–10‰ enrichment in $\delta^{34}S$ relative to associated gypsum (Table 5). The large isotopic difference would seem to preclude simple dissolution of gypsum and reprecipitation of the sulfate as celestite. Two mechanisms could be proposed for the genesis of barite

Table 6 Pb isotopic analyses of galena from the Sekarna deposit

Sample references	Mineral	Host rocks	$^{208}Pb/^{206}Pb$	$^{207}Pb/^{206}Pb$	$^{206}Pb/^{204}Pb$	$^{207}Pb/^{204}Pb$	$^{208}Pb/^{204}Pb$
GC	Galena	Dolomite (unit C)	2.0725	0.8352	18.7695	15.6759	38.9004
GD1	Galena	Dolomite (unit C)	2.0746	0.8362	18.7583	15.6862	38.9154
GD2	Galena	Dolomite (unit C)	2.0819	0.8371	18.8627	15.7902	39.2700
GS	Galena	Phosphorite (unit A)	2.0729	0.8357	18.7536	15.6733	38.8752
GPH	Galena	Phosphorite (unit A)	2.0713	0.8348	18.7876	15.6838	38.9154
GD3	Galena	Limestone (Campanian–Maastrichtian)	2.0701	0.8350	18.7418	15.6488	38.7976
GD4	Galena	Limestone (Campanian–Maastrichtian)	2.0763	0.8369	18.7663	15.7046	38.9642

in the Lower Metlaoui Formation: (1) hydrothermal input of Ba-enriched fluids and (2) early diagenetic formation within the sediments. The size and morphology of the barite crystals and their sulfur isotopic compositions may help discriminate between the two mechanisms.

Sekarna barite is characterized by fibroradiated concretion shapes in silicified phosphatic marls and is enriched by about 4‰ relative to Eocene seawater sulfate, reflecting barite formation from residual sulfate after preferential loss of ^{32}S to H_2S during bacterial sulfate reduction (BSR). Similar textures and isotopic patterns have been observed in Paleogene concretions in the West Carpathian Flysh in Poland (Leśniak et al. 1999), which were interpreted to reflect diagenetic processes occurring in the sediment column, including BSR. Another example was presented by Goldberg et al. (2006) who described Cambrian barite–pyrite concretions in black shales of the early Cambrian Niutitang Formation in China. Based on $\delta^{34}S$ and $\delta^{18}O$, the authors proposed a diagenetic origin for the barite after extensive BSR. In both studies, the enrichments in heavy isotopes were attributed to closed or semi-closed conditions during diagenesis in which pore water sulfate underwent extensive BSR. Barite $\delta^{34}S$ values in the Sekarna deposits vary from the coeval seawater sulfate value to higher values. The isotopic compositions of celestite and barite are thus consistent with data from the literature that show enrichment by 5–10‰ relative to the associated gypsum, which is inconsistent with the simple dissolution of preexisting sulfate minerals and reprecipitation of the sulfate as barite.

Diagenetic barite can form at the oxic–anoxic boundary in marine sediments where BSR is also taking place. At this location, sulfate-reducing bacteria metabolize isotopically light sulfate more rapidly than isotopically heavy sulfate to produce sulfide, leaving residual sulfate enriched in heavy sulfur (Seal II et al. 2000). Thus, the enrichment in the heavy isotope of sulfur may reflect the formation of barite in restricted basins with limited water exchange with the open ocean. In contrast, barites that form where Ba-rich solutions emanate directly into seawater should carry the isotopic signature of the Eocene seawater sulfate, which was around 21‰ (Claypool et al. 1980).

Sulfur source(s)

The reduced sulfur in sediment-hosted Zn–Pb ores can be derived from a variety of sources including organically bound sulfur, H_2S-bearing natural gas, contemporaneous seawater sulfate, diagenetic pyrite, and sulfate evaporite facies in the stratigraphic section. Reduction of sulfate can be accomplished by two processes: low-temperature bacterially mediated reduction (BSR) and abiotic thermochemical reduction (TSR). BSR is common in diagenetic settings, with optimal temperatures ranging from 0°C to 70±10°C; rates of reduction are drastically reduced at higher temperatures (Machel 2001). TSR requires higher temperatures, >100°C, and is more efficient above 125°C (Ohmoto 1992).

At Sekarna, $\delta^{34}S$ values for sphalerite and galena are negative, falling in the relatively narrow range (from −16.0‰ to −9.3‰), with sphalerite $\delta^{34}S$ values higher, on average, than galena values. The uniformity of the isotopic compositions, and the fact that sphalerite $\delta^{34}S$ is generally greater than galena $\delta^{34}S$, suggests that H_2S had been homogenized in the ore-forming fluid and that sphalerite and galena precipitation involved fluid–mineral isotopic exchange that approached, although may not have attained, isotopic equilibrium. The low (negative) $\delta^{34}S$ values suggest that sulfate reduction occurred in locations, perhaps pore waters of anoxic sediments, that were in communication with a large sulfate reservoir perhaps overlying seawater.

The high $\delta^{34}S$ value of Sekarna barite (25.1±0.2‰) is generally consistent with a seawater origin for the sulfate (Claypool et al. 1980). The $\delta^{34}S$ of Palaeogene seawater sulfate, which has been determined from the analyses of evaporates and marine barite, was about 21‰ (Claypool et al. 1980; Paytan et al. 1998). Gypsum precipitated from seawater will have an isotopic composition that is higher than the dissolved sulfate by 1.65±0.12‰ (Thode and Monster 1965). There is no significant fractionation associated with the dissolution of sulfates, but repeated dissolution and reprecipitation of older sulfates could lead to a significant increase in $\delta^{34}S$ relative to the marine value. We prefer an interpretation in which the high Sekarna barite values (average=25.1‰, n=2) reflect isotopic enrichment of sulfate as a consequence of BSR.

The isotopic fractionation associated with sulfate reduction that produced the Sekarna sulfides was about 33‰ (21‰ difference between Eocene marine sulfate (Ayora et al. 1995; Paytan et al. 1998) and ore sulfides (average= −11.8‰)). This fractionation is close to the average difference between seawater sulfate and sedimentary sulfides of the same age (40‰; Ohmoto 1986). The similarity of barite $\delta^{34}S$ values to the Tertiary marine sulfate value suggests that barite sulfur was derived from Tertiary evaporite minerals or sulfate contained in pore water in surrounding sedimentary units.

Phosphorite-hosted mineralization displays textural evidence that sulfides replaced earlier barite (barite is found as submicroscopic inclusions in sphalerite and galena). Thus, sulfur for ore formation may have been derived from a reductive dissolution of barite as well as from Eocene evaporites or seawater. Diagenetic pyrite was not a major sulfur source. Although anoxic sediments of the Cenomanian–Turonian Bahloul Formation are strongly enriched in diagenetic pyrite, this sulfur is much lighter, with $\delta^{34}S$ values of −18±2‰ (Peevler et al. 2003). More deeply buried Triassic evaporites could also have been a source of sulfur, as

proposed for several deposits in northern Tunisia (Sheppard and Charef 1990; Orgeval 1994; Sheppard et al. 1996; Bouhlel 1993, 2005, Bouhlel et al. 2007). Reduction of deeply buried marine sulfate is commonly interpreted to involve TSR and to result in positive $\delta^{34}S$ values for ore minerals. However, it is important to note that positive isotopic values can also result from closed-system BSR, as well as from the mixing of sulfur from multiple sources involving multiple reduction processes.

Fluid inclusion temperatures within the ore zone are permissive of TSR acting on local sulfate, but the low and uniform sulfide $\delta^{34}S$ values at Sekarna suggest a homogeneous fluid source and do not support the involvement of TSR in ore genesis. It is unlikely that sphalerites containing both the moderate-salinity and high-salinity inclusion types precipitated from two distinct fluids. Stretching during post-entrapment overheating can be excluded because the low-salinity fluid inclusions show the highest homogenization temperatures. The temperature of sulfide deposition exceeded the temperature range at which bacterial processes are efficient. BSR must have occurred at a different place and/or time relative to sulfide deposition. It is quite possible that sulfate was reduced by bacterial processes, and then the resulting H_2S mobilized by higher temperature brines to form sphalerite and galena. Reaction between dissolved H_2S and metallic chloride complexes in mixing and diffusion zones resulted in rapid sulfide precipitation.

Conclusions

The Sekarna sulfide deposit occurs within an organic-rich phosphatic host rock that differs from the host rocks for most MVT deposits. The deposit shows predominantly late diagenetic to epigenetic styles of mineralization that replaced carbonate cement. Mineral assemblages are simple and are dominated by sphalerite, galena, Fe sulfides, and minor barite. The ore-forming fluids were brines of moderate salinity and temperature. The minor element geochemistry of Sekarna galena and sphalerite resembles the minor element geochemistry of sulfides in carbonate-hosted MVT deposits elsewhere in the world.

The sulfur isotopic compositions of Sekarna sulfides are relatively uniform; the data are interpreted to reflect a single sulfur source that most likely involved BSR acting on Eocene marine sulfate. The Pb isotopic compositions of galena are also relatively uniform. The data suggest that the ore fluids circulated through deep levels of the upper crust.

Similarities to MVT deposits include the simple mineralogy, late diagenetic to epigenetic timing of mineralization, sulfide replacement of carbonate, and the involvement of basinal brines. However, the uniform sulfur and Pb isotopic compositions observed at Sekarna, which imply a single metal source, are atypical of MVT deposits.

Acknowledgments This paper is part of a Doctorate thesis of the first author. We would like to express our thanks to Sheldon A. Skaggs (Department of Geology, Building University of Georgia Athens) for lead isotope analyses. We wish to thank Karen Duttweiler Kelley (USGS, Denver USA) for constructive comments and for English edits. We are grateful to Christian Marignac for the editorial handling and his effort to improve this article. Yves Fuchs and Etienne Delloul, two reviewers of this article, are gratefully acknowledged for their critical and constructive comments that helped significantly improve the manuscript. Bernd Lehmann, editor-in-chief of the journal, is thanked for his constructive comments on the article. S. Bouhlel gratefully acknowledges support by Fulbright Scholar Grant that made possible the carbon, oxygen, and sulfur analysis at the USGS Denver, USA.

References

Altschuler ZS (1980) The geochemistry of trace elements in marine phosphorites. Part I. Characteristic abundances and enrichment. In: Bentor YK (ed) Marine phosphorites. SEPM Special Publication, vol 28, pp 19–30

Ayora C, Taberner C, Pierre C, Pueyo JJ (1995) Modelling the sulfur and oxygen isotopic composition of sulfates through a halite-potash sequence: implications for the hydrological evolution of the Upper Eocene South Pyrenean Basin. Geochim Cosmochim Acta 59:1799–1808

Bains S, Norris RD, Corfield RM, Faul KL (2000) Termination of global warmth at the Paleocene/Eocene boundary through productivity feedback. Nature 407:171–174

Barca D, De Francesco AM, Crisci GM (2007) Application of laser ablation ICP-MS for characterization of obsidian fragments from Peri-Tyrrhenian area. J Cultural Herit 8:141–150

Baturin GN (1982) Phosphorites on the seafloor: origin, composition and distribution. Elsevier, Amsterdam, 343 pp

Béji-Sassi A (1999) Les phosphates dans les bassins paléogènes de la partie méridionale de l'Axe Nord-Sud (Tunisie). Unpublished thesis Doctorat d'Etat ès-Sciences Géologiques, Université Tunis II, Tunisia, 424 pp

Béji-Sassi A, Sassi S (1999) Le cadmium associé aux dépôts phosphatés en Tunisie méridionale. J Afr Earth Sci 29:501–513

Bodnar RJ (1993) Revised equation and table for determining the freezing point depression of H_2O–NaCl solution. Geochim Cosmochim Acta 57:683–684

Boni M, Gilg HA, Aversa G, Balassone G (2003) The "Calamine" of SW Sardinia (Italy): geology, mineralogy and stable isotope geochemistry of a supergene Zn-mineralization. Econ Geol 98:731–748

Bonnefous J, Bismuth H (1982) Les faciès carbonatés de plateforme de l'Eocène moyen et supérieur dans l'offshore Tunisien nord-oriental et en mer pélagienne. Implications paléogéographiques et analyse micropaléontologique. Bull Cent Rech Explor Prod Elf-Aquitaine 6(2):337–407

Bouhlel S (1993) Gîtologie, minéralogie et essai de modélisation des minéralisations de Pb–Zn–Sr–Ba–F–(S°) associées aux carbonates jurassiques et crétacés et aux diapirs triasiques (Tunisie septentrionale). Unpublished thesis Doctorat d'Etat ès-Sciences Géologiques, Université Tunis II, Tunisie, 293 pp

Bouhlel S (2005) Carbonate-hosted Mississippi Valley-type Pb–Zn deposits in Tunisia (Eastern Atlasic belt). Proceedings of the 8th Biennial SGA Meeting, vol 3, Beijing China, pp 19–22

Bouhlel S, Johnson CA, Leach DL (2007) The peridiapiric-type Pb–Zn deposit at Fedj El Adoum, Tunisia: geology, petrography, and stable isotopes. Proceedings of the Ninth Biennial SGA Meeting, Dublin, Ireland, pp 323–325

Bouhlel S, Leach DL, Johnson CA, Lehmann B (2009) Ore textures and isotope signatures of the peridiapiric carbonate-hosted Pb–Zn deposit of Bougrine, Tunisia. Proceedings of the Tenth Biennial SGA Meeting, vol 1, Townsville, Australia, pp 409–411

Bréhéret JG, Brumsack HJ (2000) Barite concretions as evidence of pauses in sedimentation in the Marnes Bleues Formation of the Vocontian Basin (SE France). Sed Geol 130:205–228

Brunett WC, Roe KY, Piper DZ (1983) Upwelling and phosphorite formation in the ocean. In: Suess E, Thiede J (eds) Coastal upwelling, its sediment record, part B. Plenum, New York, pp 377–397

Burollet PF, Odin JL (1980) Paléocène en Tunisie-Pétrole et phosphate. In: Géologie comparée des gisements de phosphate et de pétrole. Documents du BRGM, pp 1–116

Burollet PF, Memmi L, M'Rabet A (1983) Le Crétacé inférieur de Tunisie. Aperçu stratigraphique et sédimentologique. Zitteliana 10:255–264

Chaabani F (1995) Dynamique de la partie orientale du bassin de Gafsa au Crétacé et au Paléogène. Etude minéralogique et géochimique de la série phosphatée éocène. Tunisie méridionale. Unpublished thesis Doctorat d'Etat ès-Sciences Géologiques, Université Tunis II, Tunisie, 428 pp

Claypool Ge, Hosler WT, Kaplan IR, Sakai H, Zak I (1980) The age curves of sulfur and oxygen isotopes in marine sulfate and their mutual interpretation. Chem Geol 28:199–260

Coppola V, Boni M, Gilg HA, Balassone G, Dejonghe L (2008) The "Calamine" nonsulfide Zn–Pb deposits of Belgium: petrographical, mineralogical and geochemical characterization. Ore Geol Rev 33:187–210

Coppola V, Boni M, Gilg HA, Strzelska-Smakowska B (2009) Nonsulfide zinc deposits in the Silesia–Cracow district, Southern Poland. Miner Deposita 44:559–580

Crawford ML (1981) Phase equilibria in aqueous fluid inclusions. Mineralogical Association of Canada short Course Handbook 6, pp 21–28

Dejonghe L, Fairon-Demaret M, Gauthier B, Streel M (1987) Détermination par analyse palynologique de l'âge Crétacé inférieur de mise en place du gisement de barite de Fleurus (Synclinorium de Namur, Belgique). C R Acad Sci 304(6):227–232

Föllmi KB (1990) Condensation and phosphogenesis: example of the Helvetic mid-Cretaceous (northern Tethyan margin). In: Notholt AJG, Jarvis I (eds) Phosphorite research and development, 52. Geological Society of London Special Publication, pp 237–252

Froelich PN, Arthur MA, Brunett WC, Deakin M, Hensley V, Jahnke R, Kaul L, Kim KH, Roe K, Soutar A, Vathakano C (1988) Early diagenesis of organic matter in Peru continental margin sediments: phosphorite precipitation. Mar Geol 80:309–343

Fuchs Y (1973) Sur les relations entre émersion et concentration métallifère (quelques exemples tunisiens). Ann Mine Geol, Tunis 26:479–509

Giesemann A, Jager HJ, Norman AL, Krouse HR, Brand WA (1994) On-line sulfur isotope determination using an elemental analyzer coupled to a mass spectrometer. Anal Chem 66:2816–2819

Gilg HA, Boni M (2004a) Role of stable isotope studies on Zn and Pb carbonates in mineral exploration of large non-sulphide deposits. 32nd International Geological Congress, 2004, Abs.Vol., pt. 2 abs 245-12, 1105 pp

Gilg HA, Boni M (2004b) Stable isotope studies on Zn and Pb carbonates: could they play a role in mineral exploration? Proceedings of ICAM 2004:4

Gilg HA, Boni M, Hochleitner R, Struck U (2008) Stable isotope geochemistry of carbonate minerals in supergene oxidation zones of Zn–Pb deposits. Ore Geol Rev 33:117–133

Goldberg T, Mazumdar A, Strauss H, Shields G (2006) Insights from stable S and O isotopes into biogeochemical processes and genesis of Lower Cambrian barite–pyrite concretions of South China. Org Geochem 37:1278–1288

Hagni RD (1983) Minor elements in Mississippi Valley-type ore deposits. In: Shanks WC (ed) Cameron volume on unconventional mineral deposits. American Institute of Mining, Metallurgical and Petroleum Engineers, Society of Mining Engineers, New York, pp 71–88

Hall WE, Heyl AV (1968) Distribution of minor elements in ore and host rock, Illinois–Kentucky fluorine district and upper Mississippi Valley zinc–lead district. Econ Geol 63:655–670

Jarvis I (1992) Sedimentology, geochemistry and origin of phosphatic chalks: the Upper Cretaceous deposits of NW Europe. Sedimentology 39:55–97

Jauzein A (1967) Contribution à l'étude géologique des confins de la dorsal Tunisienne (Tunisie septentrionale). Ann Mine Geol, Tunis 22:475

Jolly JL, Heyl AV (1968) Mercury and other trace-elements in sphalerite and wall-rocks from central Kentucky, Tennessee, and Appalachian zinc districts. U S Geol Surv Bull 1252-F:1–29

Krajewski KP, Van Cappellen P, Trichet J, Kuhn O, Lucas J, Martin-Algarra A, Prevot L, Tewari VC, Gaspar L, Knight RI, Lamboy M (1994) Biological processes and apatite formation in sedimentary environments. Eclogae Geo Helv 87:701–745

Leach DL, Sangster DF, Kelly KD, Large RR, Carven G, Allen CR, Gutzmen J, Walters S (2005) Sediment-hosted lead–zinc deposits: a global perspective. Economic Geology 100th Anniversary volume, pp 561–607

Leśniak PM, Łącka B, Hladíkova J, Zieliński G (1999) Origin of barite concretions in the West Carpathian flysch, Poland. Chem Geol 158:155–163

Liu T, Lin Y, Chen G (1999) Geochemical characteristics of the independent cadmium deposit, Niujiaotang, Duyun, Guizhou. Chinese Sci Bull 44:61–63

Machel HG (2001) Bacterial and thermochemical sulfate reduction in diagenetic setting—old and new insights. Sed Geol 140:143–175

McArthur JM, Walsh JN (1984) Rare-earth geochemistry of phosphorites. Chem Geol 47:191–220

McCrea JM (1950) On the isotopic chemistry of carbonates and a paleotemperature scale. J Chem Phys 1:849–857

McLennan SM (1989) Rare earth elements in sedimentary rocks: influence of provenance and sedimentary processes. In: Lipin BR, McKay GA (eds) Geochemistry and mineralogy of rare earth elements, vol 21. Mineralogical Society of America Reviews in Mineralogy, pp 169–200

Monteiro LVS, Bettencourt JS, Juliani C, De Oliveira TF (2006) Geology, petrography, and mineral chemistry of the Vazante non-sulfide and Ambrósia and Fagundes sulfide-rich carbonate-hosted Zn–(Pb) deposits, Minas Gerais, Brazil. Ore Geol Rev 28:201–234

Nathan Y, Benaliouhaj N, Prévôt L, Lucas J (1996) The geochemistry of cadmium in the phosphate-rich and organic rich sediments of the Oulad-Abdoun and Timahdit basins (Morocco). J Afr Earth Sci 22:17–27

Nathan Y, Soudry D, Levy Y, Shitrit D, Dorfman E (1997) Geochemistry of cadmium in the Negev phosphorites. Chem Geol 142:87–107

Ohmoto H (1986) Stable isotope geochemistry of ore deposits. Rev Min 16:491–559

Ohmoto H (1992) Biogeochemistry of sulfur and the mechanisms of sulfide–sulfate mineralization in Archean oceans. In: Schidlowski M, Golubic S, Kimberley MM, Mckirdy DM, Trudinger PA (eds)

Early organic evolution: implications for mineral and energy resources. Springer, Berlin, pp 378–397

Orgeval JJ (1994) Peridiapiric metal concentration: example of the Bou Grine deposit (Tunisian Atlas). In Fontboté L, Boni M (eds) Sediment-hosted Zn–Pb ores. Special Publication No. 10 Soc. Geo. Applied to Mineral Deposits. Springer, Berlin, pp 354–389

Orgeval JJ, Giot D, Karoui J, Monthel J, Sahli R (1989) The discovery and investigation of the Bou Grine Pb–Zn deposits (Tunisian Atlas). Chronique de la recherche minière. Special Issue 1989:53–68

Ounis A, Kocsis L, Chaabani F, Pfeifer HR (2008) Rare earth elements and stable isotope geochemistry ($\delta^{13}C$ and $\delta^{18}O$) of phosphorite deposits in the Gafsa Basin, Tunisia. Palaeogeogr Palaeoclimatol Palaeoecol 268:1–18

Paytan A, Kastner M, Campbell D, Thiemens MH (1998) Sulfate sulfur isotopic composition of Cenozoic seawater. Science 282:1459–1461

Peevler J, Fayek M, Misra KC, Riciputi LR (2003) Sulfur isotope microanalysis of sphalerite by SIMS: constraints on the genesis of Mississippi valley-type mineralization, from the Mascot-Jefferson City district, East Tennessee. J Geochem Explor 80:277–296

Perthuisot V, Hatina N, Rouvier H, Steinberg M (1987) Concentration métallique (Pb–Zn) sous un sur-plomb diapirique: Exemple de Jebel Bou Khil (Tunisie Septentrionale). Bull Soc Géol Fr 8:1153–1160

Ramkumar M, Harting M, Stüben D (2005) Barium anomaly preceding K/T boundary: possible causes and implications on end Cretaceous events of K/T sections in Cauvery Basin (India), Israel, NE-Mexico and Guatemala. Int J Earth Sci (Geol Rundsch) 94:475–489

Reynard B, Lécuyer C, Grandjean P (1999) Crystal-chemical controls on rare earth element concentrations in fossil biogenic apatites and implications for paleoenviromental reconstructions. Chem Geol 155:233–241

Roedder E (1984) Fluid inclusions. Mineral Soc Am Rev Miner 12:644

Rouvier R, Perthuisot V, Mansouri A (1985) Pb–Zn deposits and salt bearing diapirs in southern Europe and North Africa. Econ Geol 80:666–687

Sainfeld P (1952) Les gîtes plombo-zincifères de Tunisie. Ann Mine Geol, Tunis 9:285

Sassi S (1974) La sédimentation phosphatée au Paléocène dans le Sud et le Centre Ouest de la Tunisie. Unpublished thesis Doctorat d'Etat ès-Sciences, Orsay Paris France, 300 pp

Sassi S (1980) Contexte paléogéographique des dépôts phosphatés en Tunisie. Géologie comparée des gisements de phosphates et de Pétrole. Documents du BRGM 24:167–183

Schmitz B, Charisi SD, Thompson EI, Speijer RP (1997) Barium, SiO_2 (excess), and P_2O_5 as proxies of biological productivity in the Middle East during the Palaeocene and the latest Palaeocene benthic extinction event. Terra Nova 9:95–99

Seal II RR, Alpers CN, Rye RO (2000) Stable isotope systematics of sulfate minerals. In: Alpers CN, Jambor JL, Nordstrom DK (eds) Sulfate minerals: crystallography, geochemistry, and environmental significance. Reviews in Mineralogy and Geochemistry 40, pp 541–593

Shepherd TJ, Rankin AH, Alderton DHM (1985) A practical guide to fluid inclusion studies. Blackie and Son, London, 239 pp

Sheppard S, Charef A (1990) Isotopic studies (H, C, O, S, Pb) on carbonate-shale hosted Pb–Zn deposits. Mobilité et concentration des métaux de base dans les couvertures sédimentaires. Manifestations, mécanismes, prospection. Documents du BRGM 183:37–49

Sheppard SMF, Charef A, Bouhlel S (1996) Diapirs and Zn–Pb mineralizations: a general model based on Tunisian (N. Africa) and Gulf Coast (U.S.A). Soc Eco Geol. Spec Pub 4:230–243

Shields G, Stille P (2001) Diagenetic constraints on the use of cerium anomalies as palaeoseawater redox proxies: an isotopic and REE study of Cambrian phosphorites. Chem Geol 175:29–48

Skaggs SA (2010) A lead isotope analysis of the provenance of defixiones (curse tablets) from Roman Carthage, Tunisia. PhD thesis, University of Georgia, 132 pp

Soliman MF (1998) Mineralogical, geochemical, and stratigraphical investigations on the Cretaceous/Tertiary (K/T) boundary sediments of the Nile Valley, Red Sea Coast, and Western Desert, Egypt. PhD thesis, Heidelberg, Germany, Ruprecht-Karls-Universitit, Heidelberg, 175 pp

Song XX (1984) Minor elements and ore genesis of the Fankou lead–zinc deposit, China. Miner Depos 19:95–104

Thode HG, Monster J (1965) Sulfur isotope geochemistry of petroleum, evaporates and ancient seas. In: Young A, Galley JE (eds) Fluids in subsurface environments. APG Mem 4, pp 367–377

Winnock E (1980) Les dépôts de l'éocène au Nord de l'Afrique : aperçu paléogéographique de l'ensemble. In: Géologie comparée des gisements de phosphates et de pétrole. Colloque International, Orléans, 6–7 Novembre 1979, Documents du BRGM 24:219–243

Yan J, Carlson EH (2003) Nodular celestite in the Chihsia Formation (Middle Permian) of south China. Sedimentology 50(2):265–278

Zaïer A (1999) Evolution tectno-sédimentaire du bassin phosphate du centre-Ouest de la Tunisie minéralogie, pétrographie, géochimie et genèse des phosphorites. Unpublished thesis Doctorat d'Etat ès-Sciences Géologiques, Université Tunis II, Tunisia, 370 pp

Zaïer A, Béji-Sassi A, Sassi S, Moody RTJ (1998) Basin evolution and deposition during the Early Paleogene in Tunisia. Petroleum Geology of North Africa. Geol Soc London, Spec Publi 132:375–393

Zartman RE, Doe BR (1981) Plumbotectonics—the model. Tectonophysics 75:135–162